

Minimum variance guided wave imaging in a quasi-isotropic composite plate

James S. Hall¹, Peter McKeon², L. Satyanarayan², Jennifer E. Michaels¹, Nico F. Declercq², and Yves H. Berthelot²

¹School of Electrical and Computer Engineering,
Georgia Institute of Technology, Atlanta, Georgia 30332-0250

²Georgia Institute of Technology, UMI Georgia Tech – CNRS 2958,
George W. Woodruff School of Mechanical Engineering,
Georgia Tech Lorraine, 2 rue Marconi, 57070 Metz-Technopole, France

Email: jennifer.michaels@ece.gatech.edu

Abstract. Ultrasonic guided waves are capable of rapidly interrogating large, plate-like structures for both nondestructive evaluation (NDE) and structural health monitoring (SHM) applications. Distributed sparse arrays of inexpensive piezoelectric transducers offer a cost-effective way to automate the interrogation process. However, the sparse nature of the array limits the amount of information available to perform damage detection and localization. Minimum variance techniques have been incorporated into guided wave imaging to reduce the magnitude of imaging artifacts and improve imaging performance for sparse array SHM applications. The ability of these techniques to improve imaging performance is related to the accuracy of *a priori* model assumptions, such as scattering characteristics and dispersion. This paper reports the application of minimum variance imaging under slightly inaccurate model assumptions, such as are expected in realistic environments. Specifically, the imaging algorithm assumes an isotropic, non-dispersive, single mode propagating environment with a scattering field independent of incident angle and frequency. In actuality, the composite material considered here is not only slightly anisotropic and dispersive but also supports multiple propagating modes, and additionally, the scattering field is dependent on incident angle, scattered angle, and frequency. An isotropic propagation velocity is estimated via calibration prior to imaging to implement the non-dispersive model assumption. Imaging performance is presented under these inaccurate assumptions to demonstrate the robustness of minimum variance imaging to common sources of imaging artifacts.

PACS. 43.20.Fn, 43.35.Zc, 43.40.Le, 43.60.Fg, 43.60.Lq, 43.60.Mn

1. Introduction

Guided waves are capable of propagating throughout large, plate-like structures and interacting with both surface and sub-surface defects. As such, distributed sparse arrays of inexpensive, piezoelectric transducers have been proposed as a cost-effective alternative to traditional bulk wave c-scans for structural health monitoring (SHM) of large, plate-like structures [1]. Obtaining comparable information from guided wave sparse arrays is made challenging by the fact that recorded signals typically have a large number of reflections from geometric scattering and guided wave propagation is both multimodal and dispersive by nature. Guided wave imaging techniques, such as elliptical (or delay-and-sum) [2,3] and hyperbolic imaging [4,5], have been shown to be capable of

overcoming these challenges to detect and localize damage sites in experimental tests. The images produced with these methods typically also contain imaging artifacts that cannot be distinguished from additional damage. The imaging artifacts can be due to a number of factors, including uncompensated dispersion, geometric reflections, multiple propagating modes, and inaccurate *a priori* assumptions, such as propagation velocity, scattering behavior, and transducer placement.

Recently, minimum variance techniques have been incorporated into the conventional elliptical imaging algorithm to successfully reduce undesired imaging artifacts [6-8]. In these studies, imaging performance improves as additional information is incorporated into the imaging algorithm. For example, if incident waves can be assumed to interact with a potential defect in a specific

manner, then imaging performance is improved. Additionally, further imaging improvement can be obtained if phase information is incorporated into the imaging algorithm. In realistic environments, however, the scattering behavior of potential defects may not be known *a priori* and sufficient information may not be available to enable effective use of phase information. A description of minimum variance imaging, referred to as MVDR imaging, is provided in Section 4.2 of this paper.

To date, much of the work with guided wave imaging algorithms has been applied to isotropic media, such as aluminum plates, in a non-dispersive frequency regime. However, carbon-fiber reinforced plastics (CFRP) are in widespread use in modern aerospace structures. As with all plate-like structures, these materials are dispersive and capable of supporting multiple propagating modes. In addition, CFRP materials also exhibit some degree of anisotropy, even for a quasi-isotropic layup, meaning that the dispersive nature of the material is direction-dependent.

This paper demonstrates the robustness of minimum variance imaging to inaccurate assumptions about the propagating environment. Specifically the algorithm assumes an isotropic, non-dispersive, single mode propagating environment with a scattering field solely dependent on the difference between incident and scattered angles. In reality, however, the propagating environment is slightly anisotropic and dispersive, two propagating modes are present, and the scattering field is dependent on incident angle, scattered angle, and frequency. The ability of guided wave imaging algorithms to successfully detect and localize damage in realistic materials, such as aerospace-quality, quasi-isotropic CFRP, and under slightly inaccurate assumptions, such as the case considered in this paper, is critical to the adoption of distributed sparse arrays for SHM.

This study is organized as follows. A brief background on the problem is presented, followed by the experimental setup and specific techniques used to calibrate the propagation velocity and perform guided wave imaging. Results are shown and discussed, and conclusions are drawn.

2. Background

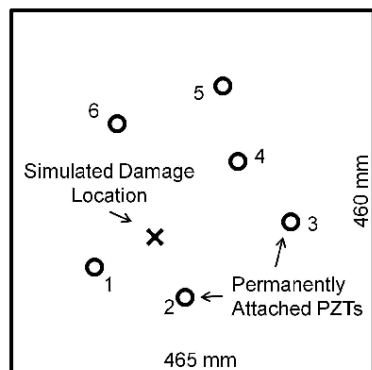
Tomographic, time-of-flight (ToF), and elliptical imaging algorithms have all been previously applied to damage localization using a distributed array of sensors. This

section provides a brief synopsis of these methods and their application to anisotropic media.

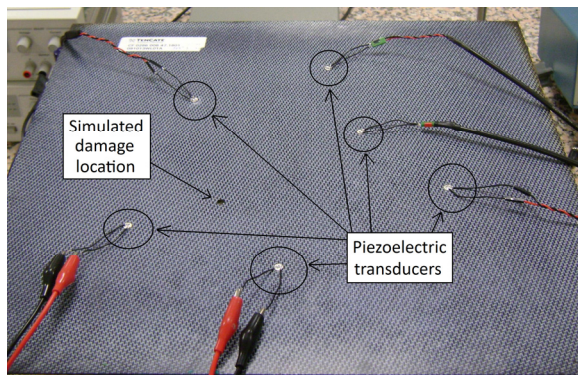
Several variations of tomographic imaging techniques have been shown to successfully detect and localize delaminations and corrosion in anisotropic media. These techniques rely on the assumption that damage causes a change in arrival time of a specific propagating mode. They vary based on the sensor pattern [9-11], signal features used to quantify velocity changes [12], diffraction assumptions [13], and image generation method [14,15]. Although tomographic techniques *can* be used with a small number of sensors, imaging quality is highly dependent on the number of recorded signals and reported results are often shown with the input of thousands of signals, which is orders of magnitude more than would be available with envisioned sparse arrays. Techniques such as the reconstruction algorithm for probabilistic inspection of damage (RAPID) method [16] have been used successfully with far fewer sensors than traditional tomographic methods by employing signal comparisons relative to baseline, or damage-free signals, and spatially distributing the corresponding signal difference coefficients.

ToF techniques typically use a small number of sensors and generate damage maps based on the assumption that scattering and possibly mode conversion occur when a guided wave interacts with damage (e.g., an incident S_0 mode scatters a portion of the incident energy as an SH_0 mode [17]). The difference in the time-of-arrival between the direct arrival and scattered signal, which can be measured by several different techniques [18,19], is used to estimate the scattered signal's propagation distance. The estimated propagation distances are then used in a localization algorithm to identify the scattering location [20-23]. Although these techniques have been successfully employed under laboratory conditions, the measurement of discrete arrival times is a non-trivial task. The measurement can be complicated, or even prohibited, by the overlap between the direct arrival and scattered signals, interference from geometric reflections, and dispersive effects.

An alternative to the above approaches is the use of elliptical or hyperbola imaging algorithms. These methods use the relationship between back-propagated signals to construct an image of the interrogation area, and typically operate on differenced signals (i.e., baseline signals from the damage-free condition are subtracted from current signals). Back-propagation can either be performed in non-dispersive media as a simple time shift, or in



(a)



(b)

Figure 1. (a) Diagram of the CFRP panel showing the pattern of permanently attached PZTs and the location of simulated damage. (b) Photograph of the experimental setup.

dispersive media with dispersion compensation [24,25]. Elliptical techniques construct images using signals from transmitter-receiver transducer pairs to localize damage along an ellipse with the transducers located at the foci of the ellipse [2,3]. Alternatively, the hyperbola technique [4,5] uses triplets of a transmitter and two receivers to localize damage along a hyperbolic curve based on the location of the two receivers. Note that for anisotropic media, the elliptical and hyperbolic nomenclature is somewhat misleading since the direction-dependent propagation velocities result in non-elliptical and non-hyperbolic loci. For the purposes of this paper, however, the quasi-isotropic nature of the material allows it to be treated as isotropic without undue performance degradation.

One variation of elliptical imaging, MVDR imaging [6-8], incorporates Minimum Variance Distortionless Response (MVDR) [26], also known as Capon's method [27], into the pixel calculation to minimize undesired artifacts. This technique expands the utility of traditional elliptical techniques by improving robustness to the complexities of the guided waves and providing better imaging performance with a small number of transducers [6-8].

3. Experiment

Experiments were performed using an aerospace-quality CFRP composite panel provided by TenCate [28] to demonstrate the proposed imaging algorithm. The quasi-isotropic layup was $[0/90/-45/45]_2$ of carbon fiber.

An array of six piezoelectric transducers (PZT) was attached to the composite plate with household super-glue

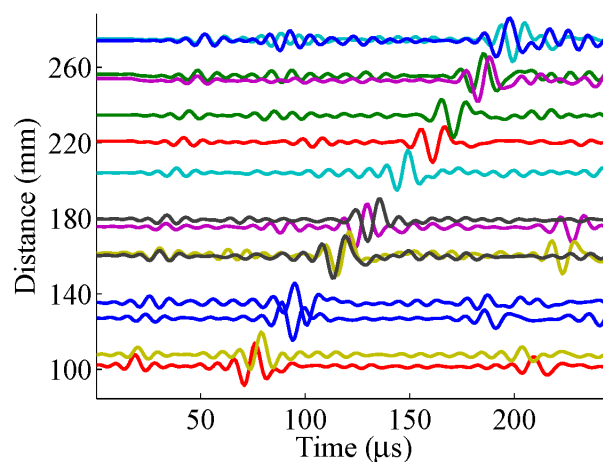


Figure 2. Waterfall plot of filtered baseline signals recorded from the sparse array. Two propagating modes can be

in an arbitrary pattern as shown in figure 1. Baseline signals were collected from the 15 unique transmitter-receiver pairs prior to the introduction of any damage. For each transmitter-receiver pair, the transmitter was excited by a spike pulse generated by an Olympus® Panametrics 5072PR pulser-receiver and recorded with a LeCroy WaveRunner 64Xi oscilloscope. The use of a spike pulse provides additional flexibility when working with experimental data in that both narrowband and broadband signals with arbitrary bandwidths and center frequencies can be isolated during post-processing. Post-processing and imaging were performed with a PC running the MathWorks MATLAB® software package. A waterfall plot of the baseline signals after low pass filtering is shown in figure 2. Note that the vertical axis is the separation

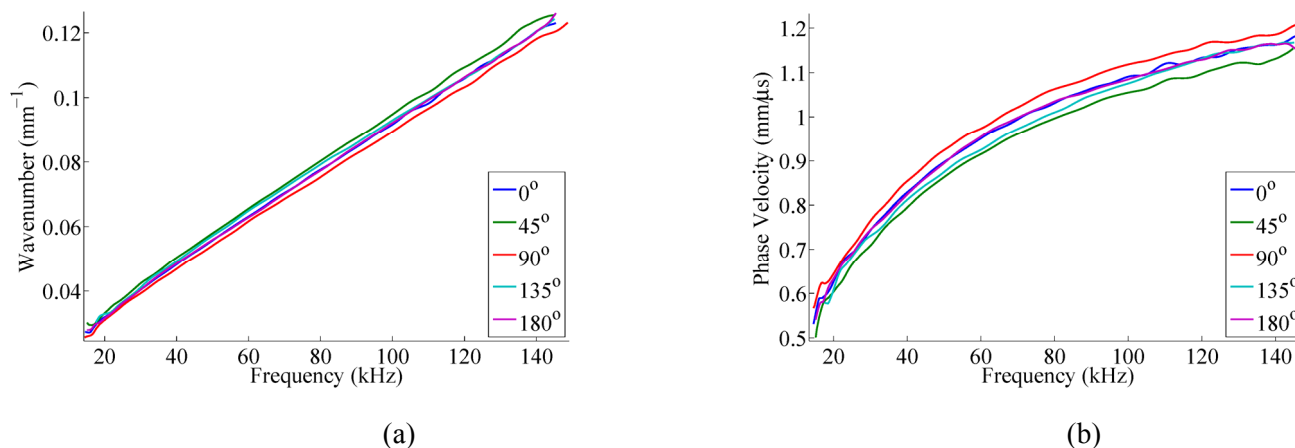


Figure 3. Dispersion measurements for five different directions of propagation of the A_0 mode shown as (a) wavenumber vs. frequency and (b) phase velocity vs frequency. Similar wavenumber slopes imply a similar group velocity for each direction.

distance between the transmitter and receiver corresponding to each recorded signal.

After recording the baseline signals, simulated damage was introduced in the form of a 5 mm diameter through-hole at the location depicted in figure 1. Although the imaging algorithm is compatible with any type of defect, a through-hole was selected as simulated damage because of the ability to describe the scattering behavior using low-order approximations [29]. Test signals were then recorded from each of the 15 transmitter-receiver pairs on the damaged plate.

4. Algorithm

This section describes the proposed imaging algorithm as applied to a quasi-isotropic CFRP panel. The overall approach is first introduced and details about velocity calibration and MVDR imaging are then provided.

Two propagating modes can be clearly observed in figure 2. The first mode arrives between 25 and 50 μs and, based on the measured propagation velocity, is believed to correspond to the fundamental symmetric mode, S_0 , while the second mode, believed to correspond to the fundamental antisymmetric mode, A_0 , arrives between 75 and 200 μs . Unfiltered, the signal amplitudes of each mode are approximately equal. A low-pass filter with a cutoff frequency of 100 kHz is applied to both the baseline and test signals to maximize the amplitude ratio between the A_0 and S_0 modes. Unfortunately, since the two modes have overlapping spectral content, they cannot be completely separated from one another by filtering. It

should be noted that figure 2 is a plot of the received signals *after* filtering.

The A_0 mode shown in figure 2 is dispersive and thus changes shape as it propagates over distance. Since the medium is anisotropic, the dispersive nature of the signals is expected to be direction-dependent. To check this assumption, dispersion was estimated along five different directions at 45° increments using data recorded by a laser vibrometer and the model-based parameter estimation method described in [30]. Figure 3 illustrates that, as expected, the phase velocity and wavenumber are dependent on propagation direction. Because these measurements were made at 45° increments on a $[0/90/-45/45]_2$ quasi-isotropic layup, the maximum directional variations present in the plate may exceed those shown in the figure. Since the slope of the wavenumber is similar for each direction, the group velocities are expected to be similar for all directions. The group velocity used for guided wave imaging is obtained from the array data using a calibration technique discussed in Section 4.1.

Prior to performing MVDR imaging, the filtered baseline signals are subtracted from the filtered test signals to isolate the scattered signals caused by damage. These baseline-subtracted signals are referred to as differenced signals throughout this paper. Ideally, if no damage is present, then the test signals are identical to the baseline signals and the differenced signals are identically zero. MVDR imaging is performed with these differenced signals. The details of MVDR imaging are discussed in Section 4.2.

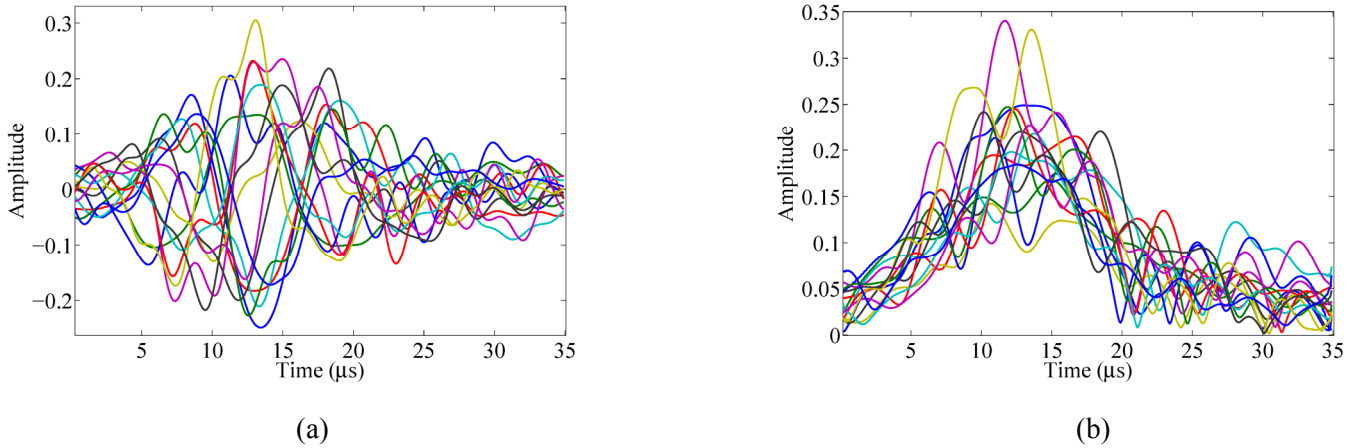


Figure 4. Back-propagated signals using a time shift based on a frequency- and direction-independent group velocity. The filtered signals are shown in (a) and the envelope of the filtered signals in (b).

4.1 Group Velocity Calibration

Calibration is performed with the filtered baseline signals to obtain an estimate of the group velocity at the time of testing. The calibration technique consists of shifting each of the received signals to the left, or back-propagating the signals, an amount of time calculated as the measured propagation distance divided by the group velocity. The group velocity that allows for the maximum agreement between back-propagated signals is chosen for use in the imaging algorithm. In other words, the group velocity, c_g , is selected to maximize

$$c_g = \arg \max_c \int_{t_1}^{t_2} \sum_{m=1}^M \left| \hat{b}_m \left(t + \frac{d_m}{c} \right) \right| dt, \quad (1)$$

where M is the number of unique transmitter-receiver pairs, $\hat{b}_m(t)$ is the analytic representation, or complex envelope, of the m th filtered, baseline signal, and d_m is the distance from the transmitter to receiver for the m th transmitter-receiver pair. The absolute value of the complex envelope of the signal, or the envelope of the signal, is used during calibration to minimize the effects of dispersion since the changing shape of the signal prevents agreement between back-propagated signals. The integration period is selected to correspond to the excitation window, which corresponds to 0-25 μ s. The optimal group velocities are found to be 5.2 mm/ μ s for the faster S_0 mode and 1.4 mm/ μ s for the slower A_0 mode.

Figure 4 illustrates the back-propagated direct arrival signals for the A_0 mode using a group velocity of 1.4 mm/ μ s. Figure 4(a), highlights the level of complexity

present in the received signals due to dispersion and geometric reflections from the S_0 and A_0 modes. Figure 4(b) shows the improved signal agreement obtained by using the envelope of the signals.

4.2 MVDR Imaging

MVDR imaging calculates each pixel value separately using the filtered, differenced signals. In Hall and Michaels [6], the pixel intensity for pixel location (x,y) is calculated as:

$$P_{xy} = \bar{\mathbf{w}}_{xy}^{-H} \mathbf{R}_{xy} \bar{\mathbf{w}}_{xy}, \quad (2)$$

where the superscript ‘‘H’’ represents the conjugate transpose, $\bar{\mathbf{w}}_{xy}$ is a vector of weights, and \mathbf{R}_{xy} is a correlation matrix of the envelope of the differenced and back-propagated signals,

$$\mathbf{R}_{xy} = \int_{t_1}^{t_2} \bar{\mathbf{r}}_{xy}(t) \bar{\mathbf{r}}_{xy}^H(t) dt. \quad (3)$$

In the above equation, t_1 and t_2 correspond to a fixed integration interval that is common to all pixel values, and the $\bar{\mathbf{r}}_{xy}(t)$ vector is constructed as:

$$\bar{\mathbf{r}}_{xy}(t) = \left[\hat{r}_1 \left(t + \frac{d_{1,xy}}{c_g} \right) \quad \dots \quad \hat{r}_M \left(t + \frac{d_{M,xy}}{c_g} \right) \right]^T, \quad (4)$$

where $d_{m,xy}$ is the total distance from the transmitter to pixel location (x,y) to receiver for the m th transmitter-receiver

pair, $\hat{r}_m(t)$ is the complex envelope of the m th differenced signal, and c_g is the propagation velocity determined during calibration. Since reflected waves in a differenced signal are dispersive, the envelopes of the differenced signals are used in the imaging algorithm to minimize the effects of the changing signal shape, allowing the imaging algorithm to handle the signals as though they were non-dispersive. Note that the time-shift applied to each element of $\vec{r}_{xy}(t)$ is specific to both the transducer-receiver pair and the pixel location.

If damage is present at location (x,y) , then each of the back-propagated signals in the $\vec{r}_{xy}(t)$ vector are aligned in time and vary in magnitude based on the scattering characteristics of the reflector and the inverse square-root of the propagation distance product, meaning that:

$$\vec{r}_{xy}(t) \sim \begin{bmatrix} \frac{\psi_{1xy}}{\sqrt{d_{1xy}^*}} & \dots & \frac{\psi_{Mxy}}{\sqrt{d_{Mxy}^*}} \end{bmatrix}^T, \quad (5)$$

where d_{mxy}^* is the product of the distances from the transmitter to pixel location and from pixel location to receiver for the m th transmitter receiver pair, and ψ_{mxy} is a scattering coefficient that characterizes the amount of energy scattered by a defect at location (x,y) for the m th transmitter-receiver pair. The distance product is appropriate to account for the geometric spreading that results from a point-like scatterer at the pixel location. As a starting point, energy is assumed to be reflected uniformly at point (x,y) , so the ψ_{mxy} values can be set to 1. Notice that if $\vec{r}_{xy}(t)$ has the relationship described in (5), then the pixel value in (2) is maximized when the weight vector, \vec{w}_{xy} , is proportional to $\vec{r}_{xy}(t)$.

For conventional elliptical imaging as implemented here, the weight vector of (2) is a unit-norm vector selected to maximize the pixel value:

$$\vec{w}_{xy}^{DS} \sim \begin{bmatrix} \frac{\psi_{1xy}}{\sqrt{d_{1xy}^*}} & \dots & \frac{\psi_{Mxy}}{\sqrt{d_{Mxy}^*}} \end{bmatrix}. \quad (6)$$

In contrast, MVDR imaging selects the weight vector, \vec{w}_{xy}^{MV} , that minimizes the pixel value subject to a constraint that maximizes the pixel value at damage

locations. Specifically, the weights are selected to satisfy the following constrained optimization problem:

$$\vec{w}_{xy}^{MV} = \arg \min_{\vec{w}} \vec{w}^H \mathbf{R}_{xy} \vec{w} \quad \text{such that} \quad \vec{w}^H \vec{e}_{xy} = 1, \quad (7)$$

where \vec{e}_{xy} is a unit-length vector, referred to as the steering vector, that describes the anticipated relationship between signals. For example, for the case where the relationship between signals can be described as in (5), the \vec{e}_{xy} vector is identical to the delay-and-sum weight vector, \vec{w}_{xy}^{DS} , defined in (6). Note that, as with the back-propagated signal vector, $\vec{r}_{xy}(t)$, the \vec{e}_{xy} vector is specific to the pixel location.

The weights that satisfy (7) can be found using a Lagrange multiplier [31]:

$$\vec{w}_{xy}^{MV} = \frac{R_{xy}^{-1} \vec{e}_{xy}}{\vec{e}_{xy}^H R_{xy}^{-1} \vec{e}_{xy}}. \quad (8)$$

In Hall and Michaels [6], it is shown that this method for selecting the weight values is effective for reducing imaging artifacts because all pixel values are minimized unless $\vec{r}_{xy}(t)$ behaves according to \vec{e}_{xy} , in which case the pixel value is maximized. Since the \vec{e}_{xy} vector describes the relationship of the signals only if damage is present at pixel location (x,y) , the pixel value is maximized only at locations corresponding to damage.

Previous work [6] has found that since the non-real-time nature of SHM data collection allows noise levels to be reduced by signal averaging, imaging performance is maximized when the integration interval is minimized. Therefore, the integration period is reduced to a single point in time that corresponds to when the back-propagated signals have the greatest amplitude. Based on figure 4, the time is selected to be 12 μ s. As a consequence of reducing the integration window to an instantaneous point in time, the inversion of the correlation matrix, \mathbf{R}_{xy} , becomes ill-posed and requires regularization. As was done in [6], the regularization is achieved with diagonal loading using a weight of 0.1 times the squared norm of $\vec{r}_{xy}(\tau)$, where $\tau = 12 \mu$ s.

Figure 5 provides a side-by-side comparison of conventional elliptical imaging and MVDR imaging

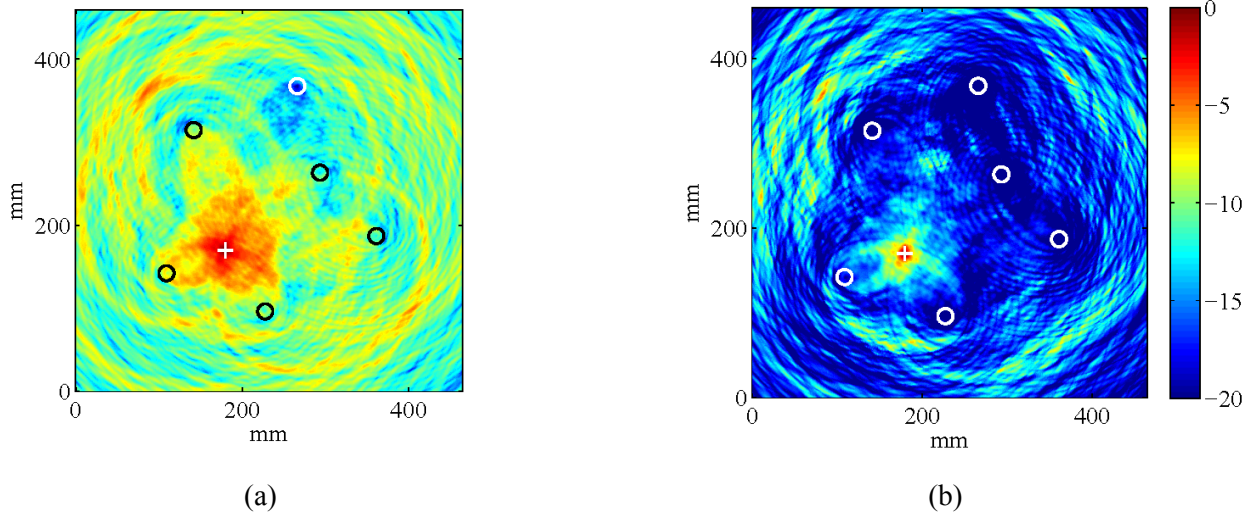


Figure 5. Guided wave imaging of CFRP panel with 5 mm diameter through-hole on a 20 dB scale. The ‘o’ symbols indicate the location of the six PZT transducers and the ‘+’ symbol designates the simulated damage location (symbol colors selected for best contrast). Images were generated using (a) conventional delay-and-sum imaging and (b) MVDR imaging.

for the CFRP plate and a 5 mm diameter through-hole. The images are color-coded according to a 20-dB scale relative to the peak pixel amplitude. The pixel values for each image were calculated using (2). The difference between the images is that the weight vector, $\bar{\mathbf{w}}_{xy}$, for figure 5(a) was calculated using (6), while the weight vector was calculated for figure 5(b) using (8).

5. Discussion

Figure 5 demonstrates the robustness of MVDR imaging using minimal *a priori* information. The images were generated using the 15 recorded signals from each of the unique transmitter-receiver pairs and a set of basic assumptions, all of which are inaccurate to some degree. The assumptions are that (1) there is a single propagating mode, (2) damage behaves as a uniform point-like scatterer (i.e., scatters equally in all directions), and (3) the medium is non-dispersive and isotropic.

Even in the presence of these inaccurate assumptions, the 5 mm diameter through-hole can be clearly observed in figure 5. The defect size is less than 1/5 of the signal wavelength ($\lambda = 28$ mm for $c_g = 1.4$ mm/ μ s and $f = 50$ kHz), which demonstrates the algorithm’s ability to detect sub-wavelength features. The imaging algorithm is expected to be sensitive to progressively smaller defect sizes with the use of higher frequencies and more accurate assumptions.

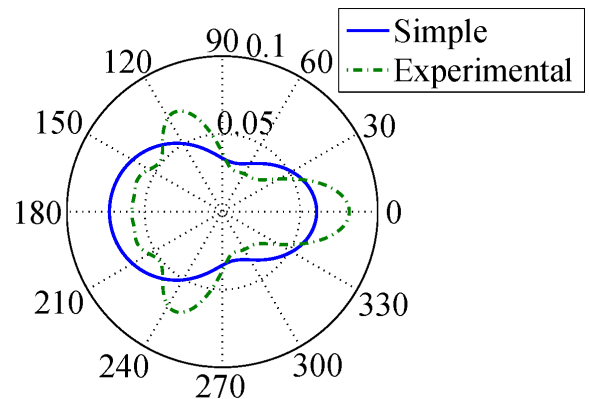


Figure 6. Two scattering fields. The “simple” scattering field is based upon a low-order approximation [29]. The “experimental” scattering field was generated using measured data and selected to maximize the pixel value at the known damage location.

Figure 2 demonstrates that there are at least two propagating modes present in the recorded signals. Beyond the filtering applied *prior to* constructing figure 2, no additional methods were used to address the presence of the S_0 mode. Therefore, any and all energy present in the S_0 mode is manifested as coherent noise in the imaging algorithm.

The assumption that potential damage scatters energy uniformly in each direction is also inaccurate. The

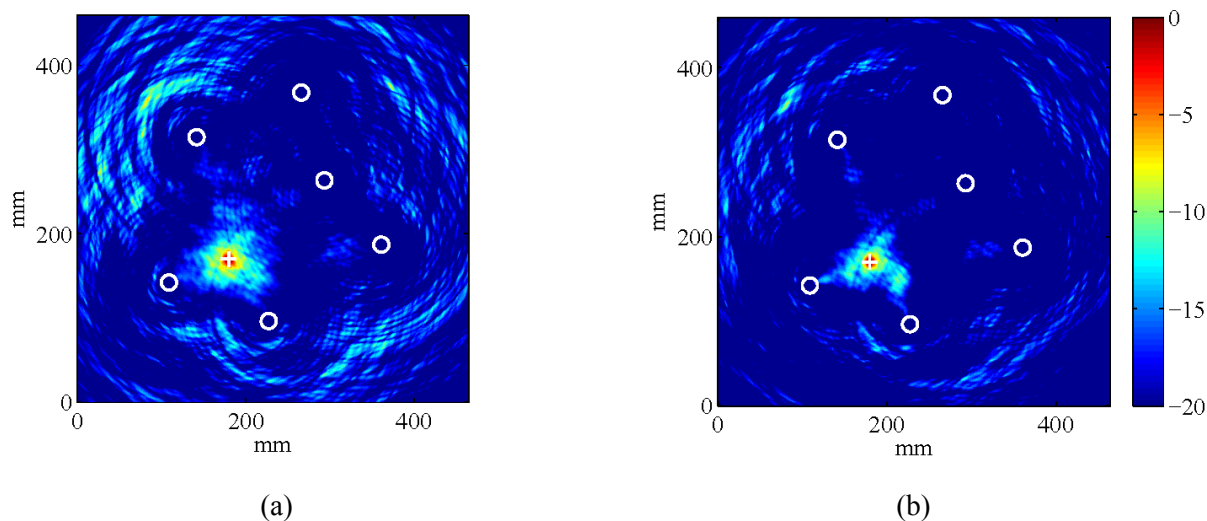


Figure 7. MVDR imaging of the CFRP panel assuming (a) the “simple” scattering field, and (b) the “experimental” scattering field (both shown in figure 6).

amplitude and phase of scattered signals are dependent on incident angle, scattered angle, and frequency. Even for a simple scatterer such as a through-hole, the scattering pattern in an anisotropic medium is specific to all three variables. An asymmetrical scatterer such as a crack may have an even more pronounced directional dependence. The discrepancy between assumed and actual behavior is minimized by the use of the envelope of the signal. Since both blocked and scattered energy results in a positive envelope value of the differenced signal, the imaging algorithm is sensitive to any scatterer, although imaging improvement is expected with a more accurate knowledge of the scattering behavior.

Although a realistic scattering field for this CFRP panel is dependent on three variables (incident angle, scattered angle, and frequency), it makes intuitive sense that a simplistic, frequency-independent scattering field based only on the difference between incident and scattered angle may be able to improve imaging performance. Figure 6 depicts two such scattering fields. The “simple” scattering field was generated analytically using low-order approximations for a homogeneous, isotropic medium [29]. The “experimental” scattering field is based on the measured data and was chosen to maximize the pixel value at the damage location. Note that the “experimental” field demonstrates the optimal imaging performance for this type of simplistic scatterer and is based on *a priori* knowledge of the damage location. Figure 7 shows the images generated using the scattering fields of figure 6. Noticeable improvement in imaging performance can be

observed between figure 5(b) and figure 7(a), and also between figures 7(a) and 7(b). The improvement results from the fact that the steering vector, \vec{e}_{xy} , is in closer agreement to the back-propagated signals in figure 7(a), and exactly matches the back-propagated signals at the damage location for figure 7(b). The imaging performance of figure 7(b) suggests that if theoretical scattering fields are unavailable, experimental characterization of scatterers may present a potential alternative.

Finally, the mismatch between the isotropic assumption and the direction-dependent dispersive nature of the material is addressed by working with the envelope of the signals and calibrating for the optimal propagation velocity. The envelope masks the effects of changing phase, and the calibration obtains a propagation velocity that avoids inaccuracies in *a priori* assumptions.

It should also be pointed out that the robustness to inaccurate assumptions obtained through the use of the signal envelope comes at the expense of imaging resolution. Hall and Michaels [6] demonstrated that the inclusion of phase information in the imaging algorithm can significantly improve imaging performance. However, MVDR imaging with phase information requires accounting for all factors affecting the phase of the signal, which includes dispersion, transducer-specific transfer functions, and scattering characteristics. The lack of scattering information was found to be the limiting factor here, since there are currently no phase specific models for the frequency and direction dependent scattering behavior

of through-holes in this specific material. Although a simplistic scattering field was used to describe the magnitude response of the through-hole, this field does not adequately describe the phase response. Therefore, additional work on modeling the scattering behavior of defects in CFRP panels is required before MVDR imaging with phase information can be performed on these materials.

6. Conclusion

Imaging in anisotropic CFRP panels can be successfully performed with minimal *a priori* information combined with minimum variance imaging, known as MVDR imaging. This paper summarizes the calibration technique and MVDR imaging algorithm used to detect and localize damage in an aerospace-quality CFRP panel with a $[0/90/-45/45]_2$ layup. As presented, the imaging algorithm inherently assumes the presence of a single, non-dispersive propagating mode with a uniform scattering field in an isotropic medium. By using the envelope of the signal to mask phase changes and MVDR imaging to reduce artifacts, the imaging algorithm was shown to be robust to the simultaneous presence of multiple propagating modes, a complicated scattering field, dispersion, and slight anisotropy. Imaging performance was shown to improve with the incorporation of a low-order approximation of scattering behavior. Further improvements can be expected with the incorporation of more accurate scattering behavior and phase information. At this time, the lack of quantitative scattering information for this material precludes the use of phase information. Future work should be directed towards characterizing the scattering field for defects of interest in CFRP material, incorporation of these scattering fields and phase information into the MVDR imaging algorithm, and application of guided wave imaging techniques with MVDR to more complicated structures, including materials with inhomogeneities and higher levels of anisotropy.

Acknowledgments

The authors would like to thank the following entities for their financial support: NASA Graduate Student Research Program (GSRP) Grant No. NNX08AY93H, the Air Force Office of Scientific Research, Grant No. FA9550-08-1-0241, Conseil Region de Lorraine, the Institut de Soudure and Georgia Tech-Lorraine. The authors would also like to acknowledge Robert Lenferink at Royal TenCate for providing the CFRP panel that was the subject of this

study. Data collection and analysis was completed at Georgia Tech Lorraine, Metz, France in the Unité Mixte Internationale Georgia Tech - CNRS UMI 2958.

References

1. J. L. Rose, "A baseline and vision of ultrasonic guided wave inspection potential," *J. Pressure Vessel Technol.*, **124** pp. 273-282 (2002).
2. C. H. Wang, J. T. Rose, and F.-K. Chang, "A synthetic time-reversal imaging method for structural health monitoring," *Smart Mater. Struct.*, **13** pp. 415-423 (2004).
3. J. E. Michaels, "Detection, localization and characterization of damage in plates with an *in situ* array of spatially distributed sensors," *Smart Mater. Struct.*, **17** (035035) (2008).
4. J. E. Michaels, A. J. Croxford, and P. D. Wilcox, "Imaging algorithms for locating damage via *in situ* ultrasonic sensors," in *IEEE Sens. Appl. Symp.*, pp. 63-67 (2008).
5. A. J. Croxford, P. D. Wilcox, and B. W. Drinkwater, "Guided wave SHM with a distributed sensor network," *Proc. SPIE*, **6935** (69350E) pp. 1-9 (2008).
6. J. S. Hall and J. E. Michaels, "Minimum variance ultrasonic imaging applied to an *in situ* sparse guided wave array," *IEEE Trans. Ultrason., Ferroelectr., Freq. Contr.*, **57** (10) pp. 2311-2323 (2010).
7. J. E. Michaels, J. S. Hall, G. Hickman, and J. Krolik, "Sparse array imaging of change-detected signals by minimum variance processing," in *Review of Progress in QNDE*, **28**, pp. 642-649 (2009).
8. J. E. Michaels, J. S. Hall, and T. E. Michaels, "Adaptive imaging of damage from changes in guided wave signals recorded from spatially distributed arrays," *Proc. SPIE*, **7295** (729515) pp. 1-11 (2009).
9. E. V. Malyarenko and M. K. Hinders, "Fan beam and double crosshole Lamb wave tomography for mapping flaws in aging aircraft structures," *J. Acoust. Soc. Am.*, **108** (4) pp. 1631-1639 (2000).
10. J. C. P. McKeon and M. K. Hinders, "Parallel projection and crosshole Lamb wave contact scanning tomography," *J. Acoust. Soc. Am.*, **106** (5) pp. 2568-2577 (1999).
11. S. M. Prasad, K. Balasubramaniam, and C. V. Krishnamurthy, "Structural health monitoring of composite structures using Lamb wave tomography," *Smart Mater. Struct.*, **13** (5) pp. N77-N79 (2004).
12. J. Hou, K. R. Leonard, and M. K. Hinders, "Automatic multi-mode Lamb wave arrival time extraction for

- improved tomographic reconstruction," *Inverse Prob.*, **20** pp. 1873-1888 (2004).
13. E. V. Malyarenko and M. K. Hinders, "Ultrasonic Lamb wave diffraction tomography," *Ultrasonics*, **39** pp. 269-281 (2001).
 14. P. M. V. Subbarao, P. Munshi, and K. Muralidhar, "Performance of iterative tomographic algorithms applied to non-destructive evaluation with limited data," *NDT & E Int.*, **30** (6) pp. 359-370 (1997).
 15. A. C. Kak and M. Slaney, *Principles of Computerized Tomographic Imaging*. (IEEE, New York, 1988).
 16. T. R. Hay, R. L. Royer, H. Gao, X. Zhao, and J. L. Rose, "A comparison of embedded sensor Lamb wave ultrasonic tomography approaches for material loss detection," *Smart Mater. Struct.*, **15** pp. 946-951 (2006).
 17. Z. Su, X. Wang, Z. Chen, L. Ye, and D. Wang, "A built-in active sensor network for health monitoring of composite structures," *Smart Mater. Struct.*, **15** pp. 1939-1949 (2006).
 18. F. Li, Z. Su, L. Ye, and G. Meng, "A correlation filtering-based matching pursuit (CF-MP) for damage identification using Lamb waves," *Smart Mater. Struct.*, **15** pp. 1585-1594 (2006).
 19. M. Lemistre and D. Balageas, "Structural health monitoring system based on diffracted Lamb wave analysis by multiresolution processing," *Smart Mater. Struct.*, **10** pp. 504-511 (2001).
 20. Z. Su, X. Wang, Z. Chen, and L. Ye, "A hierarchical data fusion scheme for identifying multi-damage in composite structures with a built-in sensor network," *Smart Mater. Struct.*, **16** pp. 2067-2079 (2007).
 21. Z. Su, L. Cheng, X. Wang, L. Yu, and C. Zhou, "Predicting delamination of composite laminates using an imaging approach," *Smart Mater. Struct.*, **18** pp. 1-8 (2009).
 22. J. Moll, R. T. Schulte, B. Hartmann, C.-P. Fritzen, and O. Nelles, "Multi-site damage localization in anisotropic plate-like structures using an active guided wave structural health monitoring system," *Smart Mater. Struct.*, **19** pp. 1-16 (2010).
 23. T. Kundu, S. Das, S. A. Martin, and K. V. Jata, "Locating point of impact in anisotropic fiber reinforced composite plates," *Ultrasonics*, **48** pp. 193-201 (2008).
 24. P. D. Wilcox, "A rapid signal processing technique to remove the effect of dispersion from guided wave signals," *IEEE Trans. Ultrason., Ferroelectr., Freq. Contr.*, **50** (4) pp. 419-427 (2003).
 25. R. Sicard, J. Goyette, and D. Zellof, "A numerical dispersion compensation technique for time recompression of Lamb wave signals," *Ultrasonics*, **40** pp. 727-732 (2002).
 26. O. L. Frost, "An algorithm for linearly constrained adaptive array processing," *Proc. IEEE*, **60** (8) pp. 926-935 (1972).
 27. J. Capon, "High-resolution frequency-wavenumber spectrum analysis," *Proc. IEEE*, **57** (8) pp. 1408-1418 (1969).
 28. Royal Ten Cate, (www.tencate.com).
 29. T. Grahn, "Lamb wave scattering from a circular partly through-thickness hole in a plate," *Wave Motion*, **37** pp. 63-80 (2003).
 30. J. S. Hall and J. E. Michaels, "A model-based approach to dispersion and parameter estimation for ultrasonic guided waves," *J. Acoust. Soc. Am.*, **127** (2) (2010).
 31. D. Johnson and D. Dudgeon, *Array Signal Processing Concepts and Techniques*. (Prentice Hall Professional, 1993).